Check for updates

# Accelerated $N_2$ reduction kinetics in hybrid interfaces of $NbTiO_4$ and nitrogen-doped carbon nanorod via synergistic electronic coupling effect

David Kumar Yesudoss [a,1], Hoje Chun [b,1], Byungchan Han [b,*], Sangaraju Shanmugam [a,*]

[a] Department of Energy Science & Engineering, Daegu Gyeongbuk Institute of Science & Technology (DGIST), Daegu 42988, Republic of Korea
[b] Department of Chemical and Biomolecular Engineering, Yonsei University, Seoul 03722, Republic of Korea

## ABSTRACT

Electrochemical ammonia synthesis through the atmospheric nitrogen reduction reaction (NRR) is a promising method for sustainable fertilizer and carbon-free hydrogen energy carriers. The inevitable selectivity gap against hydrogen evolution reaction and inert nitrogen ($N_2$) hinders the device-level usage of nitrogen cathodes. In this work, we report engineered electrocatalyst/support interface of $NbTiO_4$ nanoparticles supported on nitrogen-doped carbon nanorods ($NbTiO_4$@NCNR) to catalyze NRR. Insisted by the pitfalls to rationally design $N_2$ reduction catalysts, the strong catalyst-support interaction strategy is adapted to tune the selectivity towards NRR. Electrochemical tests reveal that $NbTiO_4$@NCNR hybrid accelerates a 10-fold increase in $N_2$ selectivity compared to pure metal oxide. Using first-principles calculations, we identify the underlying mechanism of enhanced performance: bridging bonds in the interface as electron transport channels to promote the $N_2$ reduction kinetics. Essentially, this study provides an insight into how to overcome the immense kinetic barrier of NRR using smartly engineered interfaces of hybrid materials.

## 1. Introduction

Ever since Fritz Haber's patent on the "synthesis of ammonia from its elements" it has revolutionized the world's agricultural productivity through the industrial manufacture of fertilizers along with population explosion [1]. Ammonia ($NH_3$) also plays a central role as the future clean energy carrier due to its high energy density (5.52 KWh $Kg^{-1}$) amidst environmentally friendly combustion products ($N_2$ & $H_2O$) [2,3]. The benefits of ammonia in the imminent century were foreseen by Haber. However, he failed to surmise its impact on biodiversity by generous fossil fuel consumption and $CO_2$ emissions as the process operates under harsh conditions (400–500 °C, 10–30 MPa) [4]. Due to the strong chemical stability (941 KJ $mol^{-1}$) of the triple bond of nitrogen molecule (N≡N), tremendous activation energy has to be necessarily fed to maintain the desired ammonia production rate [5,6]. Consequently, it is compelling to innovate the conventional Haber Bosch process or design a new process with a less polluting, less energy-consuming, and clean ammonia production route.

Over the last decades, the inexhaustible chemical energy resources like $N_2$ and $H_2O$ in the electrolyzers driven by renewable power sources have attracted concerted attention as alternative ways to produce $NH_3$

gas [2,3,7]. Several strategies have been focused on lowering the activation energy to the N≡N bond break and pushing the selectivity towards NRR from competing for hydrogen evolution reaction (HER) [8]. Hence, the design of effective electrocatalysts dramatically reducing the threshold for $N_2$ activation is essential to resolve the never-ending quest for $NH_3$ production.

In accordance with the conventionally known design principle, the best natural catalyst of nitrogenase comprises an $N_2$ binding catalytic molybdenum-iron activation center and electron-donating iron protein, combined producing $NH_3$ under mild conditions [9]. Therefore, mimicking the "binding-activation" mechanism as in enzymatic $N_2$ fixation was extensively studied to fabricate electrophotocatalysts for $N_2$ reduction [10–13]. To promote electron-donation into antibonding orbitals of adsorbed $N_2$, various strategies such as defect engineering, substantial doping, and hybridization have been attempted [3,4,14–17]. Some of the approaches indeed were successful for remarkable enhancement of NRR activity and stability.

On the other hand, tuning the properties of nanostructured materials by strong catalyst-support interaction can lower the activation barrier through interfacial charge transfer and stabilize the adsorbed intermediates [18–21]. The hybrid nanostructures are suitable candidates
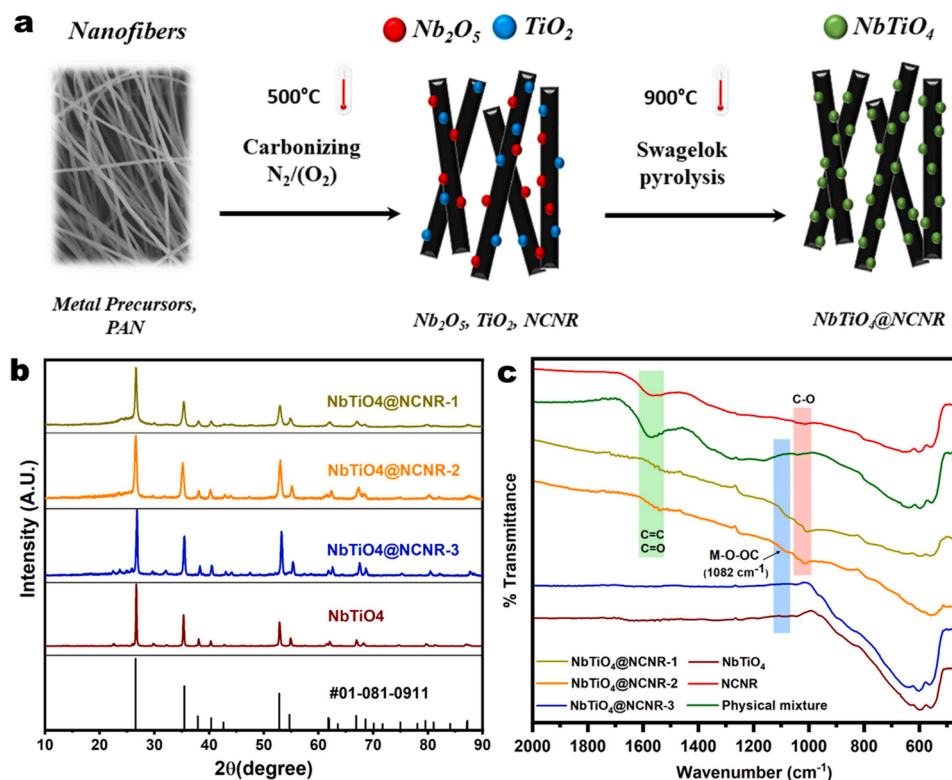
---

**Fig. 1.** (a) Schematic representation of NbTiO$_4$@NCNR synthesis process, (b) XRD patterns of NbTiO$_4$@NCNR-1, 2, 3, and NbTiO$_4$, (c) FTIR spectra of NbTiO$_4$@NCNR-1, 2, 3, NbTiO$_4$, NCNR, and physical mixture of NbTiO$_4$ & NCNR.

for tuning the electron-donating function for N$_2$ activation, notwithstanding it is less considered in designing electrocatalysts for NRR. For instance, the strong interfacial bonds between cobalt sulfide nanoparticles and graphene support accelerated the reaction kinetics for N$_2$ reduction, though the study lacks information on binding energy perturbations on the metal centers and the effect of support loading [22]. Likewise, similar studies on various heterojunctions have featured enhanced electronic coupling effect and NRR activity compared to the bare catalyst without support, indicating the significance of strong catalyst-support interaction [15–17,23–25].

Besides, the favorable adsorption of N$_2$ over protons on the electrocatalyst surface is a crucial factor determining the selectivity and faradaic efficiency. Recently, increasing attention has been paid to developing cost-effective and earth-abundant transition metal oxides as NRR catalysts, which can effectively bind the N$_2$ molecule by accepting electrons from the σ orbital and cleaving the triple bond through back donation into antibonding orbitals [25–30]. Theoretical studies have revealed the outstanding NRR stability of rutile-type metal oxides with (110) surface, and particularly, niobium oxide (NbO$_2$) exhibited favorable N$_2$ adsorption ability comparable to the noble rhenium dioxide (ReO$_2$) [31]. As reported by Huang and associates, NbO$_2$ showed an exceptional faradaic efficiency of 32%, yet a poor NH$_3$ yield rate (11.6 µg h$^{-1}$mg$^{-1}$) is a limitation for its practical application [30]. According to our knowledge, the absence of an electron boosting component can be the reason for sluggish NRR kinetics, despite the high N$_2$ selectivity of NbO$_2$. Recently, Hu et al. demonstrated the electron-donating role of Ce through synergistic charge transfer in Ce$_{1/3}$NbO$_3$, resulting in a five-fold improvement of NH$_3$ yield rate than a pristine Nb$_2$O$_5$, which implies that electron boosting elements should promote the activation of inert N$_2$ molecule [32].

Inspired by these pioneering works, *for the first time*, we demonstrate the rutile-type niobium titanium oxide nanoparticles on nitrogen-doped carbon nanorods (NbTiO$_4$@NCNR) hybrid as an effective NRR catalyst for electrochemical NH$_3$ synthesis under ambient conditions. Density

functional theory (DFT) calculations evidently show the outstanding N$_2$ adsorption ability on metal-terminated Nb-site of NbTiO$_4$ and Ti is the key acting as electron-reservoir during the N$_2$ activation. Moreover, the effect of carbon loading on the NbTiO$_4$@NCNR significantly affects the NRR activity via electron transport from the support. The strong interaction between N$_2$ binding NbTiO$_4$ catalyst center and electron contributing NCNR support imitates the binding-activation mechanism of enzymatic N$_2$ fixation.

## 2. Experimental details

Synthesis of NbTiO$_4$@NCNR involves the electrospinning of the polymer composed of Polyacrylonitrile (PAN, 1 g), Niobium oxalate (0.7 mmol), Titanium oxy acetylacetonate (0.7 mmol), and DMF (9 g). First, metal precursors and DMF were sonicated in a glass vial until uniform dispersion, followed by the addition of PAN and overnight stirring at 90 °C before electrospinning. As electrospun matt was stabilized in N$_2$ atmosphere (500 cc/min) at 250 °C for 2 h (Step-I) and carbonizing at 500 °C (Step-II). Finally, the carbon nanorods containing Nb$_2$O$_5$ and TiO$_2$ were transferred to a Swagelok and pyrolyzed at 900 °C for 6 h (Step-III) with a ramping rate of 5 °C/min to yield NbTiO$_4$@NCNR-1.

The carbon was oxidized at different levels by injecting O$_2$ gas with the nitrogen stream in step-II to expose the metal oxide supported on carbon nanorods. N$_2$/O$_2$: 450/50 mixture partially oxidized carbon from the sample (NbTiO$_4$@NCNR-2), whereas 400/100 mixture completely removed carbon resulting in one-dimensional NbTiO$_4$ nanorods (NbTiO$_4$@NCNR-3). Bulk NbTiO$_4$ was obtained by carrying out step-I & II in an open-air atmosphere. All samples were treated in a Swagelok (Step-III) after step-II, which is essential for forming single-phase NbTiO$_4$.
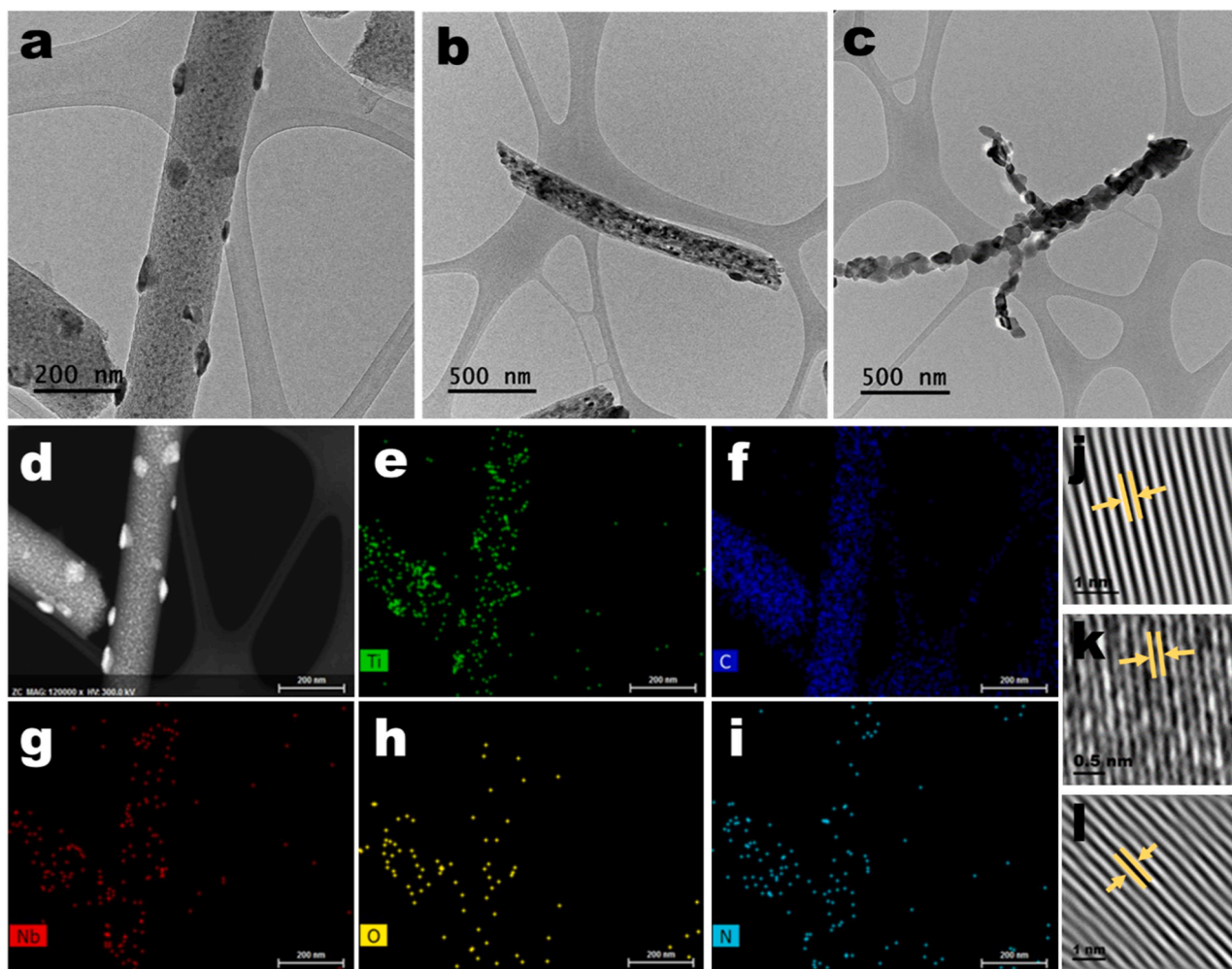
**Fig. 2.** FE-TEM images of (a) NbTiO$_4$@NCNR-1, (b) NbTiO$_4$@NCNR-2, (c) NbTiO$_4$@NCNR-3, (d–i) Elemental mapping of NbTiO$_4$@NCNR-1, (j–l) D-spacing of 0.274 nm (101), 0.175 nm (211), 0.351 nm (110).

## 3. Results and discussion

### 3.1. Structural characterization

To explore the growing interest in using transition metal oxides as N$_2$ reduction electrocatalysts, we developed unique NbTiO$_4$ nanoparticles supported on carbon nanorods by the electrospinning method as schematically depicted in Fig. 1a. X-ray Diffraction (XRD) patterns reveal the formation of a single-phase rutile structured metal oxide with space group P42/mnm in both NbTiO$_4$@NCNR hybrids and pure NbTiO$_4$ (ICSD 01-081-0911) (Fig. 1b). The broad peak in the hybrid sample around 26° originated from the graphitic carbon (002) diffraction (ICSD 01-074-2329), confirming the co-existence of carbon and NbTiO$_4$ in the hybrid catalyst. Furthermore, the crystalline nature of the metal oxide exhibits prominent diffraction peaks at 26, 35, 37, 52, and 54° indexed to the (110), (101), (200), (211), and (220) planes, respectively. The planes are then considered to build NbTiO$_4$ surface slab models for first-principles computational studies. Also, the carbon loading on the NbTiO$_4$ metal oxide was varied by partial oxidation of the carbon at different levels through passing O$_2$ during carbonization. The XRD pattern shows the single-phase NbTiO$_4$ of carbon etched samples, namely NbTiO$_4$@NCNR-2,3. Hence, the amount of carbon loading does not affect the rutile nature of the NbTiO$_4$, and the influence of electrochemical NRR performance by the crystal orientation can be ruled out.

The Raman spectra show the typical characteristic peaks of D- and G-band of carbon around 1354 cm$^{-1}$ and 1595 cm$^{-1}$, respectively, which are absent in the pristine NCNR, indicating that metal oxide aids in catalytic graphitization (Fig. S1). Additionally, four characteristic vibrational modes of rutile-type metal oxide such as B$_{1g}$, E$_g$, A$_{1g}$, and second-order effect (SOE) were observed around 120, 407, 520, and 267 cm$^{-1}$, respectively, confirming the successful formation of NbTiO$_4$ with space group P42/mnm. The occurrence of luminescence backgrounds can be attributed to the defects in the NbTiO$_4$ caused by hybridizing with carbon nanorods [33,34].

The chemical interaction between NbTiO$_4$ particles and NCNR composite was studied using FTIR (Fig. 1c). The peaks around 1020 and 1570 cm$^{-1}$ are due to C-O, C=O, C=C functional groups of the NCNR, while the typical metal-oxide-metal (M-O-M) stretching can be found at 900 cm$^{-1}$ [35,36]. In the FTIR spectrum of the NbTiO$_4$@NCNR hybrids, the appearance of a new peak at 1082 cm$^{-1}$ can be assigned to the co-valent metal-oxide-carbon bonding (M-O-OC), resulting from the conjugation effect between NbTiO$_4$ and NCNR [37]. Interestingly, the physical mixture of NbTiO$_4$ and NCNR did not exhibit the M-O-OC stretching, which indicates that the interaction only exists in the composites synthesized together in Swagelok. Also, the dramatic decrease in intensity of the C=O and M-O-M peaks compared to pristine NCNR and NbTiO$_4$ implies strong interaction between the M—O bond in NbTiO$_4$ and oxygen-containing groups in NCNR support in the hybrid catalysts.

The nature of carbon and the loading of metal oxide on carbon nanorods were analyzed by TGA analysis in the O$_2$ atmosphere. The result shows the oxidation of carbon in the range of 470–520 °C, indicating the high degree of graphitization in NbTiO$_4$@NCNR-1 (Fig. S2)
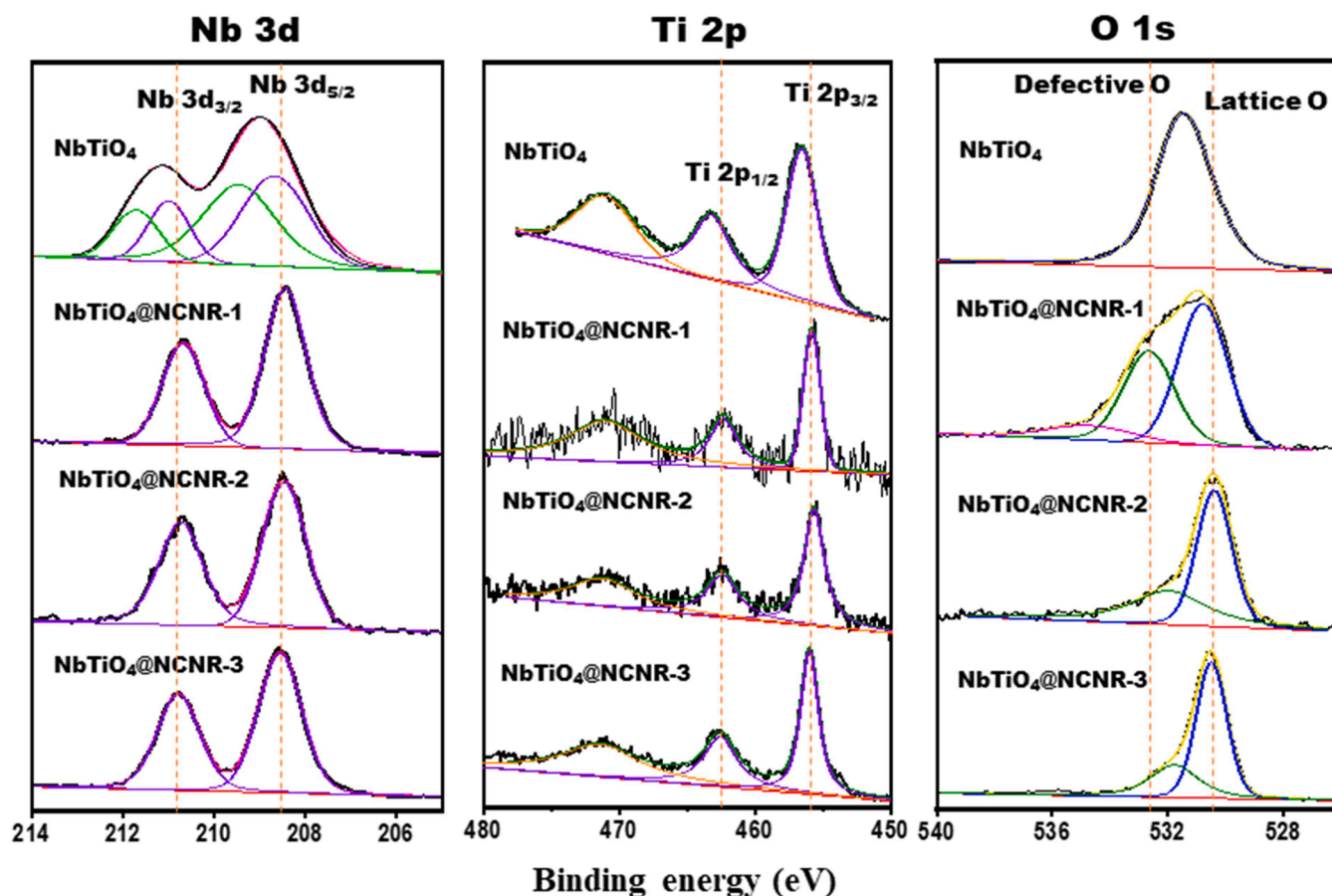
**Fig. 3.** XPS high-resolution spectrum of Nb 3d, Ti 2p, O 1s for $NbTiO_4$, $NbTiO_4$@NCNR-1, 2, 3.

[38]. Moreover, the metal oxide loading after carbon oxidation was determined to be around 40%, whereas the pristine $NbTiO_4$ has no carbon in it, and the weight gain with heat treatment is due to the dissociation of $NbTiO_4$ to $Nb_2O_5$ & $TiO_2$. To support this C, H, and N elemental analysis was carried out to measure the comprehensive elemental composition, from which the carbon content was found to be 62% (remaining metal oxide), and the carbon loading on $NbTiO_4$@NCNR-2 and -3 was found to be 34% and 0% respectively (Table S1). The BET surface area analysis revealed a high surface area of the $NbTiO_4$@NCNR hybrid catalysts (Table S2). $NbTiO_4$@NCNR-1 exhibited a type II isotherm implying the physisorption between adsorbed gas and catalyst, whereas the carbon removed samples tend to show type IV isotherm as seen in $TiO_2$ [39]. Moreover, the H3 type hysteresis loops of $NbTiO_4$@NCNR-2,3 are the characteristic of platelet-like particles (Fig. S3). Thus, the H3 hysteresis and type IV isotherm confirm the exposure of $NbTiO_4$ particles after the controlled removal of carbon.

### 3.2. Morphology analysis

The morphology of all the samples was analyzed by using field emission scanning and transmission electron microscopes. $NbTiO_4$@NCNR hybrids and NCNR exhibit similar nanorods morphology with an average diameter of 300–400 nm, whereas the pure $NbTiO_4$ morphology collapsed without carbon and remained as particles (Fig. S4 and S5). From the SEM images of $NbTiO_4$@NCNR, the metal oxide particles implanted on the surface of carbon nanorods can be observed. The exposure of metal oxide to the surface is further observed by TEM analysis (Fig. 2) which shows that the embedded $NbTiO_4$ particles on NCNR are well exposed to adsorb reactant $N_2$ for reduction.

Moreover, the $NbTiO_4$ surface shows major facets such as (101), (211), and (110) planes calculated from the D-spacing 0.274, 0.175, 0.351 nm, respectively (Fig. 2j–l). The well-dispersed nature of the $NbTiO_4$ on NCNR can be seen from the elemental mapping analysis, and some of the metal oxides are buried beneath the carbon surface (Fig. 2d–i). On the other hand, pure $NbTiO_4$ without carbon support exhibits critical agglomeration shown in Fig. S6, indicating the role of one-dimensional carbon support to keep the metal oxide separated for higher active site consumption. The etched carbon samples ($NbTiO_4$@NCNR-2,3) retained the one-dimensional structure, which can be observed from the FE-SEM and FE-TEM images (Figs. 2b and c, S5). When the pristine $NbTiO_4$ prepared by the same electrospinning method and carbon removal in the open air has collapsed particle morphology, the controlled carbon removal by mixing oxygen with inert gas produced metal oxide with a 1D structure.

### 3.3. Surface structure and chemical states analysis

The chemical composition of the $NbTiO_4$@NCNR was determined by the XPS analysis. The Nb 3d peak was deconvoluted into two components ($3d_{3/2}$ and $3d_{5/2}$) with a binding energy value of 209.9 and 207.2 eV, corresponding to the + 4 oxidation state of the Nb in $NbTiO_4$@NCNR, ensuring the complete transformation of $Nb_2O_5$ and $TiO_2$ to $NbTiO_4$ (Fig. 3). On the other hand, pure $NbTiO_4$ exhibits mixed oxidation states of + 4 and + 5 due to the presence of unconverted $Nb_2O_5$. The Ti 2p profiles in pure $NbTiO_4$ and $NbTiO_4$@NCNR hybrid reveal its + 4 oxidation state confirmed by the peaks centered at 465.5 and 459.7 eV corresponding to $2p_{1/2}$ and $2p_{3/2}$, respectively. Overall, the binding energy values of both Nb and Ti in hybrid catalysts show a downshift towards lower binding energies than pristine $NbTiO_4$,
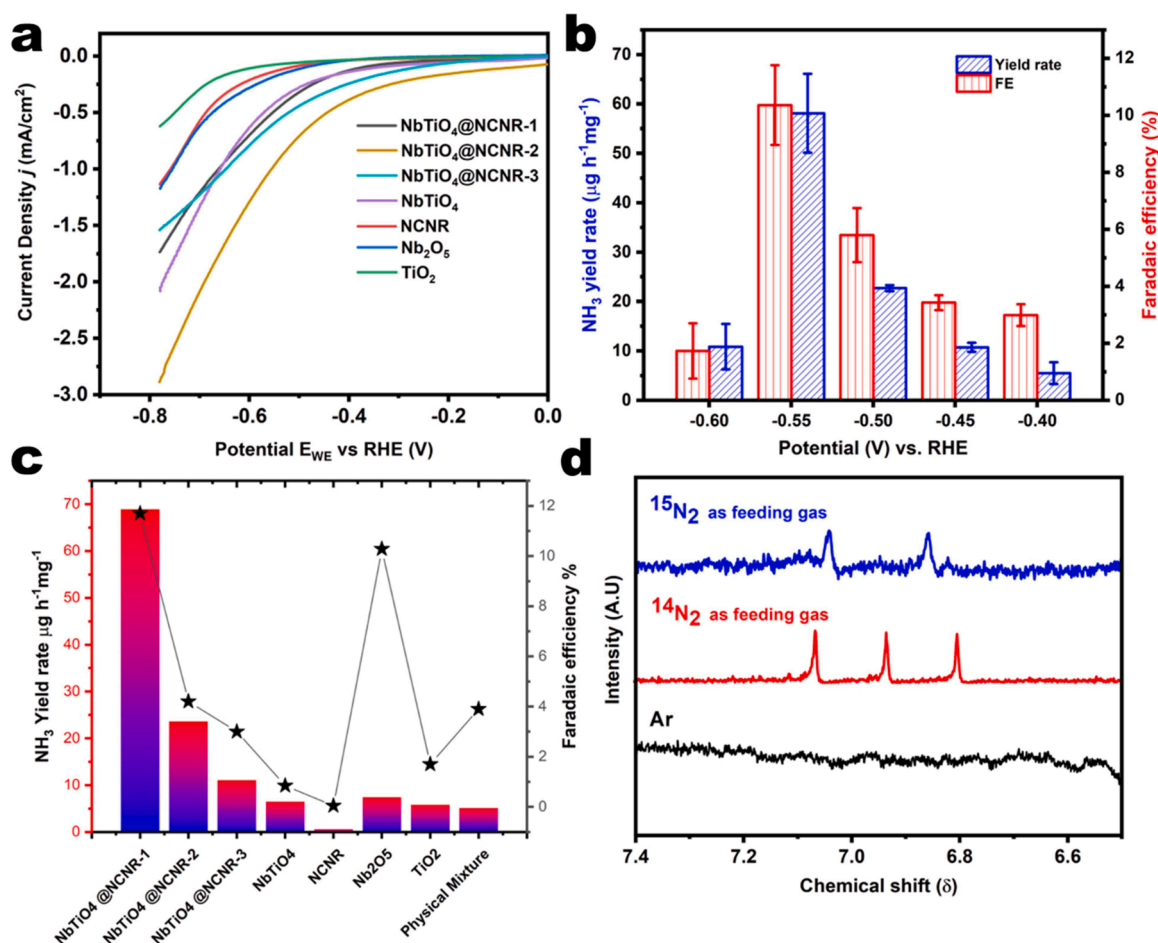
**Fig. 4.** Electrocatalytic NRR performance (a) LSV of various control samples catalysts in 0.01 M HCl, (b) $NH_3$ yield rate of $NbTiO_4$@NCNR-1 and corresponding Faradaic efficiency, (c) Overall comparison of the NRR activity of control samples at − 0.55 V vs. RHE, (d) $^{15}N$ isotope labeling test identified by $^1H$ NMR.

indicating a possible transfer of electron cloud towards metal centers gained from carbon substrate (Fig. 3) [40]. The strong catalyst-support interaction is essential for the charge transfer to occur, and the bridging bonds between them result in either positive or negative binding energy shifts. This can be validated from the O1s profile of the pristine and hybrid $NbTiO_4$ catalysts, whereas the existence of an additional peak at 532.7 eV could be attributed to the defective oxygen on the hybrid $NbTiO_4$@NCNR resulting from M-O-OC bonding [41]. Since the defective oxygen cannot be matched with the O 1s carbonyl group peak (532.17 eV) in NCNR, its existence is due to the interaction of $NbTiO_4$ with NCNR rather than the surface functionalization of carbon nanorods (Fig. S7, Table S3). Considering the carbon influences the electronic structure of the $NbTiO_4$ by advancing electrons to the metal centers, the effect of binding energy shifts by varying the carbon loading on $NbTiO_4$ was observed. The higher binding energy values of Nb and Ti metal centers in pristine $NbTiO_4$ tend to exhibit a downshift with the increase in carbon loading, and the shift magnitude is in the order of $NbTiO_4$@NCNR-1 > $NbTiO_4$@NCNR-2 > $NbTiO_4$@NCNR-3 > $NbTiO_4$ [42,43].

A concise study of the band structures was carried out to justify electron transfer phenomena through the interface of $NbTiO_4$@NCNR composites as observed by XPS analysis. Fig. S8 shows the UV-Vis DRS spectra of pristine $NbTiO_4$, NCNR, and $NbTiO_4$@NCNR-1,2,3 composites. The samples without carbon, such as $NbTiO_4$ and $NbTiO_4$@NCNR-3 exhibits comparatively less absorption in the visible light region due to the existence of a slight band-gap. However, the introduction of carbon increases absorption across the entire UV and visible region in NCNR and $NbTiO_4$@NCNR-1,2. This red-shift is associated with the formation

of M-O-OC bonding which reduces the band-gap in carbon-loaded catalysts and thus, proving the synergistic effect in $NbTiO_4$@NCNR-1,2 [36, 44].

Ultraviolet Photoelectron Spectroscopy (UPS) data shows a slight difference in the kinetic energy cut-off of the carbon-loaded samples compared to the pure $NbTiO_4$ (Fig. S9). The reduced ionization potentials in the $NbTiO_4$@NCNR composites are mostly due to the charge transfer from NCNR support [45]. Moreover, the ionization energy for eliminating valence electrons to the vacuum level is closely related to the electron cloud of the metal centers and the charge-transfer ability of the supports. Overall, the surface structure and chemical state studies conclude the fact that electron moves from the substrate towards the catalyst sites, and its magnitude depends on the amount of carbon loading on $NbTiO_4$.

### 3.4. Electrochemical nitrogen reduction reaction performance

To evaluate the electrochemical activity of the control samples, linear sweep voltammetry (LSV) was performed in 0.01 M HCl (pH = 2) at a scan rate of 10 mV s$^{-1}$. Fig. 4a shows the LSV polarization curves, in which an increase in the current density can be observed beyond − 0.4 V vs. RHE. Samples with $NbTiO_4$ show enhanced reduction current than the other control samples, and the $NbTiO_4$@NCNR-1 hybrid catalyst performs better than pristine metal oxide, indicating that carbon doping improves the electrocatalytic activity. Also, the affinity of $NbTiO_4$ towards $N_2$ adsorption was assessed preliminarily by introducing $N_2$ in the electrolyte. An improved current density in the $N_2$ saturated electrolyte compared to the Ar saturation reveals the ability of the $NbTiO_4$ and
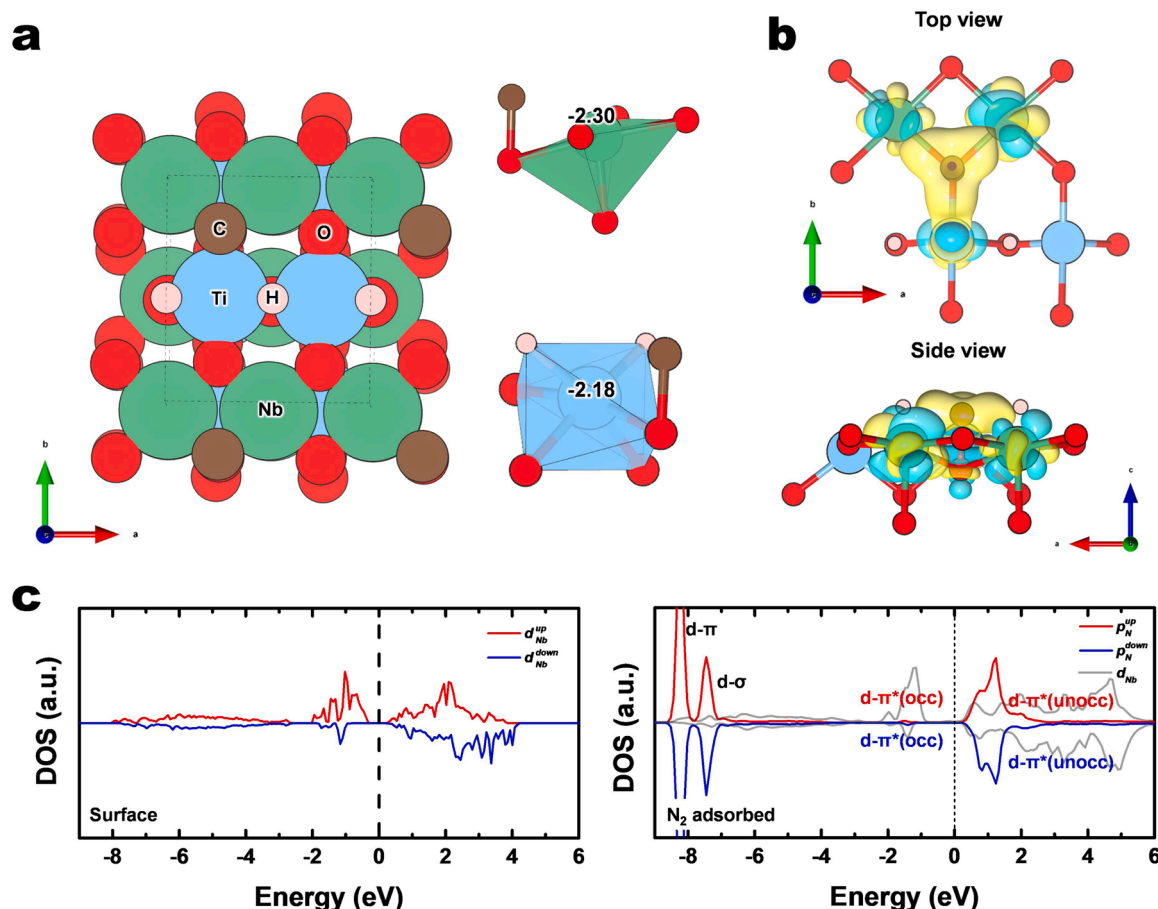
**Fig. 5.** (a) Model system NbTiO$_4$@NCNR hybrid system (left) and surface metal polyhedrons of Nb and Ti with the electron charge by Bader charge analysis (right). (b) Charge density distribution as the C introduced to NbTiO$_4$. Yellow represents the charge accumulation, and cyan represents charge depletion. (c) Projected density of states (DOS) of Nb and N before (left) and after (right) the N$_2$ adsorption for NbTiO$_4$@NCNR hybrid system.

hybrid samples towards N$_2$ activation (Fig. S10). It should be noted that the increase in current density is also accompanied by the hydrogen evolution reaction (HER), which should be suppressed by tuning the electrocatalyst for selective adsorption of N$_2$. The relatively high electrochemical activity of NbTiO$_4$@NCNR-2 and NbTiO$_4$@NCNR-3 in a cathodic can be attributed to the more exposed active sites of metal oxide, evidenced by the high double-layer capacitance (Fig. S11).

The electrocatalytic NRR performance of the NbTiO$_4$ and NbTiO$_4$@NCNR-1 were evaluated in an H-type electrolysis cell separated by the Nafion-212 membrane. Before electrolysis, the electrolyte was saturated with N$_2$ gas for 30 min and purged continuously during the electrolysis by adequately positioning the sparger near the cathode. The chronoamperometric tests were conducted in the potential range of − 0.4 to − 0.6 V vs. RHE in the N$_2$ saturated electrolyte under ambient conditions. The produced ammonia was quantified spectrophotometrically by the indophenol blue method with the help of a standard calibration curve. NH$_3$ production began at − 0.4 V for all samples and followed a volcano-type trend, and HER was active at higher potentials. The NH$_3$ yield rate and faradaic efficiency reached a maximum at − 0.55 V vs. RHE and gradually dropped due to the competitive adsorption of hydrogen ions. Among all samples, NbTiO$_4$@NCNR-1 showed the highest yield rate of 58.13 ± 8 µg h$^{-1}$mg$^{-1}$ and 10.4 ± 1.4% faradaic efficiency (Fig. 4b; Table S4), which is incredibly higher compared to the pure NbTiO$_4$ (6.08 ± 0.3 µg h$^{-1}$ mg$^{-1}$ and 0.88 ± 0.02%) (Table S5). Although the charge consumed during electrolysis was almost the same for both samples, with NbTiO$_4$ being slightly higher, the selectivity for N$_2$ adsorption varies drastically (Fig. S13a and S15a). This behavior can be attributed to the presence of

carbon in the hybrid sample, which plays a significant role in tuning the N$_2$ adsorption ability of NbTiO$_4$. However, with the decrease in carbon loading, the electrochemical NRR performance also decreased steadily.

Moreover, the shift in binding energies of the metal centers in NbTiO$_4$@NCNR-1 due to hybridization with carbon from the XPS analysis revealed the change in the electronic structure of the catalyst. At − 0.55 V vs. RHE, the NbTiO$_4$@NCNR-1 hybrid catalyst exhibited a remarkable NH$_3$ production rate and faradaic efficiency compared to the control samples such as NbTiO$_4$@NCNR-2, NbTiO$_4$@NCNR-3, NbTiO$_4$, NCNR, Nb$_2$O$_5$, and TiO$_2$ (Fig. 4c) due to high electronic conductivity derived from the carbon substrate and the strong bridging bonds between the catalyst and support, which act as electron transport channels to boost sluggish N$_2$ reduction kinetics. To further highlight the significance of catalyst-support interactions and interfacial engineering, pure NbTiO$_4$ and NCNR were mixed by grinding and tested for NRR. Apparently, the physical mixture showed poorer performance than the hybrid sample due to the lack of synergy between NbTiO$_4$ and NCNR (Fig. S17). Most importantly, it is crucial to identify the N-source responsible for NH$_3$ formation due to uncertainties caused by ubiquitous ammonia from NO$_x$, and the atmosphere [46]. The $^1$H NMR spectrum shows a triplet peak for electrolysis carried out with standard $^{14}$N as the feed gas, which when switched with $^{15}$N isotope reveals the characteristic doublet of $^{15}$NH$_3$, indicating the feed gas is consumed for reduction (Fig. 4d). Moreover, the absence of NH$_3$ resonance for argon as feeding gas confirms that no external contaminants add up to the total NH$_3$ yield rate except for the N$_2$ supplied.

We performed density functional theory (DFT) calculations to elucidate the underlying mechanism of the electronic coupling effect
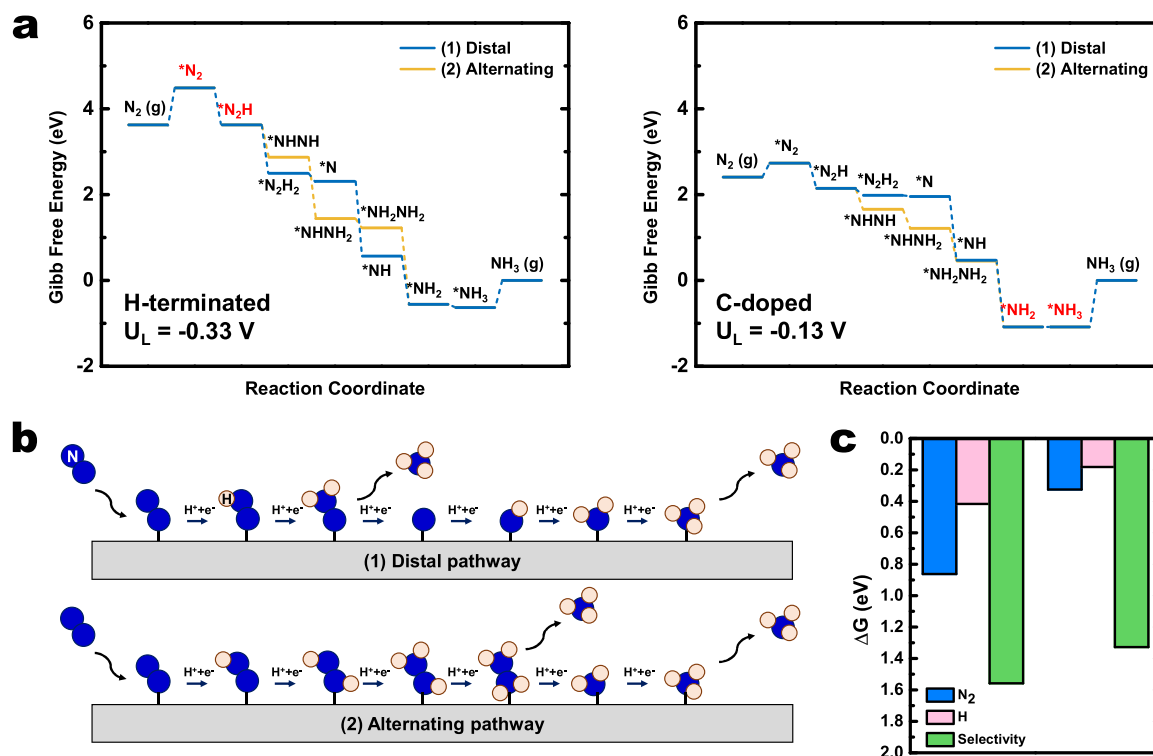
**Fig. 6.** (a) Gibbs free energy diagrams of NRR for H-terminated (left) and C-doped (right) slab models, and (b) the schematic illustration of considered reaction mechanisms. The potential determining step (PDS) is marked in red. (c) Gibbs free energy of adsorption for $N_2$ and H, and selectivity index.

between $NbTiO_4$ and carbon nanorod. We modeled the (110) surface of rutile-type $NbTiO_4$ as it was reported to be thermodynamically the most stable facets [47]. The (110) surface contains metal atoms of Nb and Ti with 5-fold coordination of O and 6-fold of four O and two H atoms, respectively (Fig. S23a) [48]. Chemical interaction of catalyst and support of $NbTiO_4$@NCNR hybrid system was modeled by introducing O≡C bonding as discussed in Fig. 1c: C atom was doped at the O site of (110) $NbTiO_4$ surface (Fig. 5a). We analyzed the variation of charge transfer at the interface in the situation. Our results indicate that the charge accumulates at C atom, which is caused by O ligand of the center metals (Nb and Ti) as it transforms into the neutral CO ligand (Fig. 5b). Bader charge analysis [49] consistently demonstrated the supplementation of charge in the surface metals (Fig. 5a and S23a). The supplementation of charge in the coordinatively unsaturated sites (cus-sites), especially for Nb ($-2.40$ e$^-$ to $-2.30$ e$^-$, the negative sign represents the electron depletion), indicates that more charge transfer facilitates $N_2$ adsorption and the subsequent catalytic reactions [50,51].

We further analyzed $N_2$ bonding activation via electronic structures after the C atom doping. The density of states (DOS) for H-terminated and C-doped $NbTiO_4$ (110) surface show that high peaks of Ti 3d orbitals appear above the Fermi level, while those of O 2p orbitals below the Fermi level (Fig. S24). It is to note that the Nb 4d orbitals near Fermi level (green arrows in Fig. S24) were observed for the C-doped $NbTiO_4$ (110) surface, indicating the high density of carriers for charge transfer in the electrochemical process. The results of charge states and electronic DOS in the cus-sites of Nb are consistent with the experimental observations of the downshift of M-O-OC binding energy. We calculated the average $d$-band center energy of surface Nb atoms to estimate the binding strengths with $N_2$. The energies for H-terminated and C-doped $NbTiO_4$ were $-4.99$ eV and $-3.87$ eV, respectively. The upshift of the $d$-band center energy of Nb indicates the stronger binding strength towards the $N_2$ than the other counterpart.

Indeed, the calculated adsorption energy of $N_2$ in the H-terminated and C-doped surfaces (0.32 eV and $-0.22$ eV, respectively) confirmed the activation of N≡N bonding by larger charge transfer from Nb in C-

doped surface than H-terminated one. The projected DOS of Nb and N after the $N_2$ adsorption elucidate the adsorption mechanism for H-terminated and C-doped $NbTiO_4$. As the $N_2$ is adsorbed, (110) $NbTiO_4$ only shows orbital hybridization of $d$-$\pi^*$ at the up spin, while C-doped (110) $NbTiO_4$ surface shows that at both up and down spins. The hybridization of $d$-$\pi^*$ in both spin up and down states signifies the easier N≡N bonding activation [52]. The charge density distributions of $N_2$ adsorption also indicate the charge transfer from Nb to the $N_2$ forming $d$-$\pi^*$ hybridization (Fig. S25).

The NRR performance of the catalyst/support hybrid was investigated by thermodynamic Gibbs free energy diagram (Fig. 6a). We considered two different reaction mechanisms (Fig. 6b) in the associative catalytic pathway (a) distal and (b) alternating one (more details in Supporting Information). The alternating pathway shows better NRR performance in both surfaces due to high adsorption strength towards N. For both pathways, $N_2$ bond length was elongated, indicating the N≡N bonding activation (Fig. S25). It is noteworthy that the reaction mechanisms in the C-doped $NbTiO_4$ surface significantly differ from the H-terminated $NbTiO_4$ one. The potential limiting step (PDS) of the H-terminated model was the first hydrogenation reaction (*$N_2$ → *$N_2H$), of which the Gibbs free energy change was 0.33 eV. This can also be detrimental on the aspect of the selectivity against the hydrogen evolution reaction. At the same time, the PDS of the C-doped model was the last hydrogenation reaction (*$NH_2$ → *$NH_3$) with the Gibbs free energy change of 0.13 eV. It indicates that the hydrogenation reactions in NRR in C-doped $NbTiO_4$ surface are thermodynamically spontaneous until the last proton/electron pair participate in, and the activation energy should also be lower than in H-terminated $NbTiO_4$ surface. It conveys that the strong interaction between support and catalyst drives large electronic charge transfer towards the nitrogenate intermediates in NRR, leading to easier N≡N bonding activation.

We evaluated the catalytic selectivity against the hydrogen production by calculating the Gibbs free energy of adsorptions and selectivity index. The selectivity index was obtained as the difference between the adsorption free energy of $\Delta G(*H)$ and $\Delta G(*N_2H)$ to evaluate the
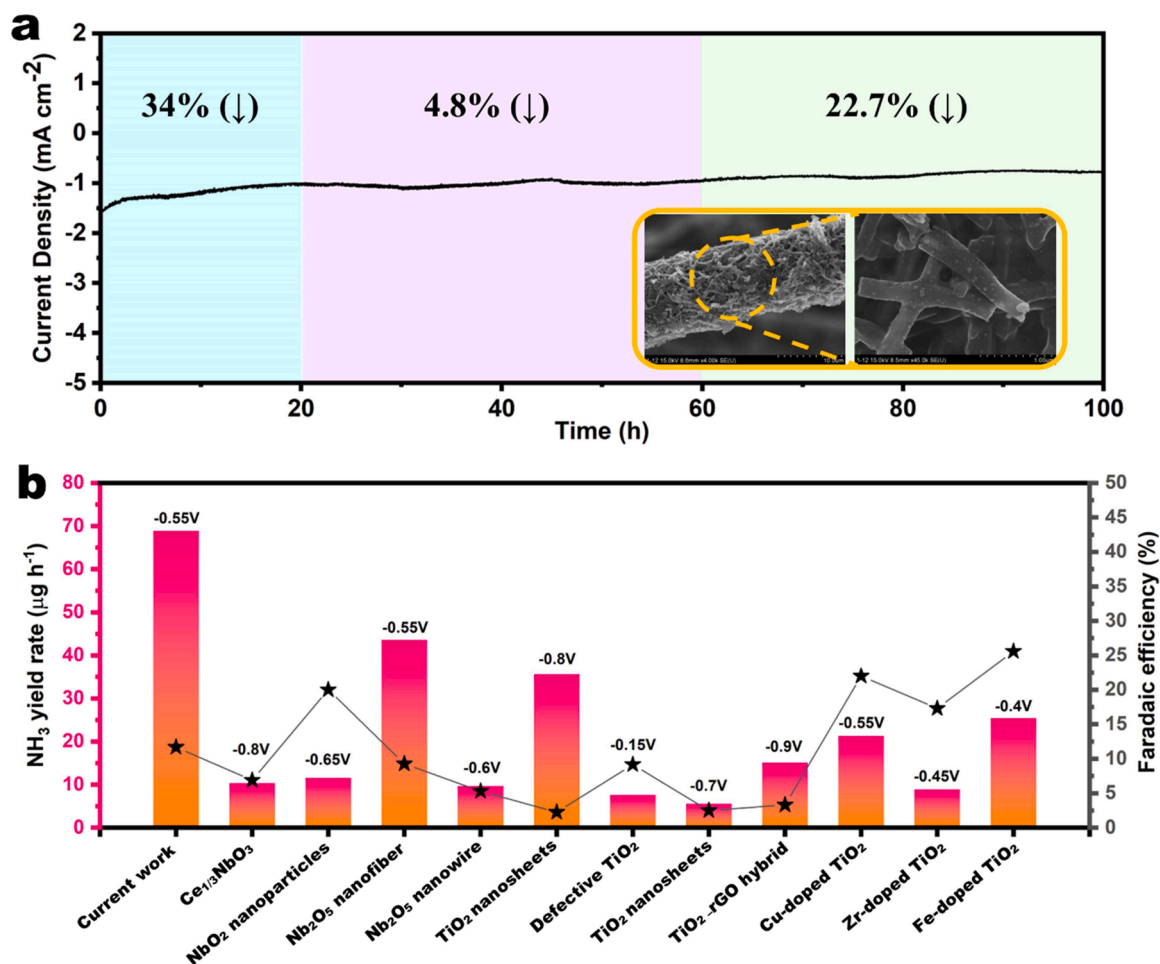
**Fig. 7.** (a) The current density of long-term 100 h durability test for NbTiO$_4$@NCNR-1 recorded at $-0.55$ V vs. RHE (Inset of figure: SEM images of the NbTiO$_4$@NCNR-1 spray-coated on carbon cloth after 100 h durability test), (b) Comparison of NH$_3$ yield rate and Faradaic efficiency with the recently reported electrocatalysts related to NbTiO$_4$@NCNR.

preference of incoming proton to the active site and to the adsorbed nitrogen. The larger the selectivity index represents, the lower selectivity since the protons are more likely to undergo the HER. It is shown that the selectivity of NRR against the HER for C-doped NbTiO$_4$ excelled that of H-terminated NbTiO$_4$. This is mainly due to the stronger binding strengths of N$_2$ and N$_2$H in C-doped NbTiO$_4$ with larger charge transfer.

The long-term durability test for NbTiO$_4$@NCNR-1 was performed by applying a constant potential of $-0.55$ V vs RHE under N$_2$ atmosphere (Fig. 7a). Initially, a maximum current density of about $-1.5$ mA cm$^{-2}$ was observed, which dynamically decreased for the first 20 h with a 34% loss in current. After that, the performance-optimized to generate a stabilized current throughout the 40 h operation followed by the degradation phase. The destruction or dissolution of one dimensional NbTiO$_4$@NCNR-1 could drastically reduce the performance; in this regard, the catalyst-coated carbon cloth electrode's SEM images after durability test shows the nanorods morphology and the NbTiO$_4$ particles on its surface. Thus, the current density loss due to the wreckage of nanorods could be ruled out, as the catalyst stands robust even after a 100 h electrolysis run. In addition, the structural stability of NbTiO$_4$@NCNR-1 was evaluated by performing post-XPS analysis, by which no significant crystallographic change can be found (Fig. S26). Nevertheless, the eccentric C 1s and O 1s profiles are due to added signals from -CF$_x$- groups of Nafion. Most importantly, the presence of graphitic-N in N 1s spectrum verifies the non-participation of doped nitrogen in overall NH$_3$ yield rate. Overall, the NbTiO$_4$@NCNR hybrid catalyst exhibits a remarkable NRR performance compared to the

recently reported Nb, Ti-based oxides, and their composites which evidently shows the significance of synergistic effects generated by hybridization (Fig. 7b).

## 4. Conclusion

NbTiO$_4$@NCNR hybrid catalysts were successfully fabricated using the electrospinning method, and the hybrid sample achieved a maximum NH$_3$ yield rate of $58.13 \pm 8$ μg h$^{-1}$mg$^{-1}$ with $10.4 \pm 1.4\%$ faradaic efficiency. The impact of carbon loading on metal oxide and its influence on NRR activity was further demonstrated by observing the synergistic effect between NCNR and NbTiO$_4$. The interfacial bridging bonds between the catalyst and support accelerated the electron transport to the metal center for donating into the anti-bonding orbital of the N$_2$ molecule, as evidenced by the dramatically decreased NRR activity when the carbon support was removed. In short, pristine NbTiO$_4$ showed the affinity for hydrogen evolution reaction, which, when hybridized with carbon, improves the selectivity for the nitrogen reduction reaction. The phenomenon of catalyst-support interactions has served as a potential catalytic activity enrichment route for various electrochemical reactions over the years, and this study contributes detailed statistics on fine-tuning the electrocatalyst/support interface for efficient electrochemical ammonia synthesis.

## CRediT authorship contribution statement

**David Kumar Yesudoss:** Conceptualization, Data curation, Formal analysis, Writing – original draft. **Hoje Chun:** Data curation, Writing – original draft. **Byungchan Han:** Supervision, Funding acquisition, Writing – review & editing. **Sangaraju Shanmugam:** Conceptualization, Funding acquisition, Supervision, Writing – review & editing.

## Declaration of Competing Interest

The authors declare that they have no known competing financial interests or personal relationships that could have appeared to influence the work reported in this paper.

## Acknowledgments

## Appendix A. Supporting information

Supplementary data associated with this article can be found in the online version at doi:10.1016/j.apcatb.2021.120938.

## References

[1] J.W. Erisman, M.A. Sutton, J. Galloway, Z. Klimont, W. Winiwarter, How a century of ammonia synthesis changed the world, Nat. Geosci. 1 (2008) 636–639, https://doi.org/10.1038/ngeo325.

[2] X. Zhao, G. Hu, C. Chen, H. Zhang, S. Zhang, H. Wang, Comprehensive understanding of the thriving ambient electrochemical nitrogen reduction reaction, Adv. Mater. (2021), 2007650, https://doi.org/10.1002/adma.202007650.

[3] X. Chen, Y. Guo, X. Du, Y. Zeng, J. Chu, C. Gong, J. Huang, C. Fan, X. Wang, J. Xiong, Atomic structure modification for electrochemical nitrogen reduction to ammonia, Adv. Energy Mater. 10 (2020), 1903172, https://doi.org/10.1002/aenm.201903172.

[4] K. Chu, F. Liu, J. Zhu, H. Fu, H. Zhu, Y. Zhu, Y. Zhang, F. Lai, T. Liu, A general strategy to boost electrocatalytic nitrogen reduction on perovskite oxides via the oxygen vacancies derived from a-site deficiency, Adv. Energy Mater. 11 (2021), 2003799, https://doi.org/10.1002/aenm.202003799.

[5] Y. Liu, X. Zhang, Z. Chen, X. Zhang, P. Tsiakaras, P.K. Shen, Electrocatalytic reduction of nitrogen on FeAg/Si for ammonia synthesis: a simple strategy for continuous regulation of faradaic efficiency by controlling H⁺ ions transfer rate, Appl. Catal. B: Environ. 283 (2021), 119606, https://doi.org/10.1016/j.apcatb.2020.119606.

[6] C. Wang, L.-L. Gu, S.-Y. Qiu, J. Gao, Y.-C. Zhang, K.-X. Wang, J.-J. Zou, P.-J. Zuo, X.-D. Zhu, Modulating CoFe₂O₄ nanocube with oxygen vacancy and carbon wrapper towards enhanced electrocatalytic nitrogen reduction to ammonia, Appl. Catal. B: Environ. 297 (2021), 120452, https://doi.org/10.1016/j.apcatb.2021.120452.

[7] G. Soloveichik, Electrochemical synthesis of ammonia as a potential alternative to the Haber–Bosch process, Nat. Catal. 2 (2019) 377–380, https://doi.org/10.1038/s41929-019-0280-0.

[8] Y. Ren, C. Yu, X. Tan, H. Huang, Q. Wei, J. Qiu, Strategies to suppress hydrogen evolution for highly selective electrocatalytic nitrogen reduction: challenges and perspectives, Energy Environ. Sci. 14 (2021) 1176–1193, https://doi.org/10.1039/D0EE03596C.

[9] H. Li, J. Shang, Z. Ai, L. Zhang, Efficient visible light nitrogen fixation with BiOBr nanosheets of oxygen vacancies on the exposed {001} facets, J. Am. Chem. Soc. 137 (2015) 6393–6399, https://doi.org/10.1021/jacs.5b03105.

[10] L. Li, J.M.P. Martirez, E.A. Carter, Prediction of highly selective electrocatalytic nitrogen reduction at low overpotential on a Mo-doped g-GaN monolayer, ACS Catal. 10 (2020) 12841–12857, https://doi.org/10.1021/acscatal.0c03140.

[11] Y. Liu, Y. Su, X. Quan, X. Fan, S. Chen, H. Yu, H. Zhao, Y. Zhang, J. Zhao, Facile ammonia synthesis from electrocatalytic N₂ reduction under ambient conditions on N-doped porous carbon, ACS Catal. 8 (2018) 1186–1191, https://doi.org/10.1021/acscatal.7b02165.

[12] H. Chen, J. Liang, L. Li, B. Zheng, Z. Feng, Z. Xu, Y. Luo, Q. Liu, X. Shi, Y. Liu, S. Gao, A.M. Asiri, Y. Wang, Q. Kong, X. Sun, Ti₂O₃ nanoparticles with Ti³⁺ sites toward efficient NH₃ electrosynthesis under ambient conditions, ACS Appl. Mater. Interfaces 13 (2021) 41715–41722, https://doi.org/10.1021/acsami.1c11872.

[13] Z. Du, J. Liang, S. Li, Z. Xu, T. Li, Q. Liu, Y. Luo, F. Zhang, Y. Liu, Q. Kong, X. Shi, B. Tang, A.M. Asiri, B. Li, X. Sun, Alkylthiol surface engineering: an effective strategy toward enhanced electrocatalytic N₂ -to-NH₃ fixation by a CoP nanoarray, J. Mater. Chem. A 9 (2021) 13861–13866, https://doi.org/10.1039/D1TA02424H.

[14] T.-N. Ye, S.-W. Park, Y. Lu, J. Li, M. Sasase, M. Kitano, T. Tada, H. Hosono, Vacancy-enabled N₂ activation for ammonia synthesis on an Ni-loaded catalyst, Nature 583 (2020) 391–395, https://doi.org/10.1038/s41586-020-2464-9.

[15] K. Chu, X. Li, Q. Li, Y. Guo, H. Zhang, Synergistic enhancement of electrocatalytic nitrogen reduction over boron nitride quantum dots decorated Nb₂CTx -MXene, Small 17 (2021), 2102363, https://doi.org/10.1002/smll.202102363.

[16] Q. Li, Y. Guo, Y. Tian, W. Liu, K. Chu, Activating VS₂ basal planes for enhanced NRR electrocatalysis: the synergistic role of S-vacancies and B dopants, J. Mater. Chem. A 8 (2020) 16195–16202, https://doi.org/10.1039/D0TA05282E.

[17] X. Li, Y. Luo, Q. Li, Y. Guo, K. Chu, Constructing an electron-rich interface over an Sb/Nb₂CTx–MXene heterojunction for enhanced electrocatalytic nitrogen reduction, J. Mater. Chem. A 9 (2021) 15955–15962, https://doi.org/10.1039/D1TA03662A.

[18] M. Ahmadi, H. Mistry, B. Roldan Cuenya, Tailoring the catalytic properties of metal nanoparticles via support interactions, J. Phys. Chem. Lett. 7 (2016) 3519–3533, https://doi.org/10.1021/acs.jpclett.6b01198.

[19] F. Polo-Garzon, T.F. Blum, Z. Bao, K. Wang, V. Fung, Z. Huang, E.E. Bickel, D. Jiang, M. Chi, Z. Wu, In situ Strong Metal–support interaction (SMSI) affects catalytic alcohol conversion, ACS Catal. 11 (2021) 1938–1945, https://doi.org/10.1021/acscatal.0c05324.

[20] S. Hosokawa, Y. Oshino, T. Tanabe, H. Koga, K. Beppu, H. Asakura, K. Teramura, T. Motohashi, M. Okumura, T. Tanaka, Strong metal–support interaction in Pd/Ca₂ AlMnO ₅₊δ: catalytic NO reduction over Mn-doped CaO shell, ACS Catal. 11 (2021) 7996–8003, https://doi.org/10.1021/acscatal.1c01559.

[21] H. Gu, G. Shi, H.-C. Chen, S. Xie, Y. Li, H. Tong, C. Yang, C. Zhu, J.T. Mefford, H. Xia, W.C. Chueh, H.M. Chen, L. Zhang, Strong catalyst–support interactions in electrochemical oxygen evolution on Ni–Fe layered double hydroxide, ACS Energy Lett. 5 (2020) 3185–3194, https://doi.org/10.1021/acsenergylett.0c01584.

[22] P. Chen, N. Zhang, S. Wang, T. Zhou, Y. Tong, C. Ao, W. Yan, L. Zhang, W. Chu, C. Wu, Y. Xie, Interfacial engineering of cobalt sulfide/graphene hybrids for highly efficient ammonia electrosynthesis, Proc. Natl. Acad. Sci. USA 116 (2019) 6635–6640, https://doi.org/10.1073/pnas.1817881116.

[23] D.K. Yesudoss, G. Lee, S. Shanmugam, Strong catalyst support interactions in defect-rich γ-Mo₂N nanoparticles loaded 2D-h-BN hybrid for highly selective nitrogen reduction reaction, Appl. Catal. B: Environ. 287 (2021), 119952, https://doi.org/10.1016/j.apcatb.2021.119952.

[24] P.-Y. Liu, K. Shi, W.-Z. Chen, R. Gao, Z.-L. Liu, H. Hao, Y.-Q. Wang, Enhanced electrocatalytic nitrogen reduction reaction performance by interfacial engineering of MOF-based sulfides FeNi₂S₄/NiS hetero-interface, Appl. Catal. B: Environ. 287 (2021), 119956, https://doi.org/10.1016/j.apcatb.2021.119956.

[25] K. Chu, Y. Liu, Y. Li, J. Wang, H. Zhang, Electronically coupled SnO₂ quantum dots and graphene for efficient nitrogen reduction reaction, ACS Appl. Mater. Interfaces 11 (2019) 31806–31815, https://doi.org/10.1021/acsami.9b08055.

[26] W. Kong, Z. Liu, J. Han, L. Xia, Y. Wang, Q. Liu, X. Shi, Y. Wu, Y. Xu, X. Sun, Ambient electrochemical N₂-to-NH₃ fixation enabled by Nb₂O₅ nanowire array, Inorg. Chem. Front. 6 (2019) 423–427, https://doi.org/10.1039/C8QI01049H.

[27] J. Han, Z. Liu, Y. Ma, G. Cui, F. Xie, F. Wang, Y. Wu, S. Gao, Y. Xu, X. Sun, Ambient N₂ fixation to NH3 at ambient conditions: using Nb₂O₅ nanofiber as a high-performance electrocatalyst, Nano Energy 52 (2018) 264–270, https://doi.org/10.1016/j.nanoen.2018.07.045.

[28] K. Chu, Y. Liu, Y. Li, Y. Guo, Y. Tian, H. Zhang, Multi-functional Mo-doping in MnO₂ nanoflowers toward efficient and robust electrocatalytic nitrogen fixation, Appl. Catal. B: Environ. 264 (2020), 118525, https://doi.org/10.1016/j.apcatb.2019.118525.

[29] K. Chu, Y. Liu, Y. Cheng, Q. Li, Synergistic boron-dopants and boron-induced oxygen vacancies in MnO₂ nanosheets to promote electrocatalytic nitrogen reduction, J. Mater. Chem. A 8 (2020) 5200–5208, https://doi.org/10.1039/D0TA00220H.

[30] L. Huang, J. Wu, P. Han, A.M. Al-Enizi, T.M. Almutairi, L. Zhang, G. Zheng, NbO₂ electrocatalyst toward 32% faradaic efficiency for N₂ fixation, Small Methods 3 (2019), 1800386, https://doi.org/10.1002/smtd.201800386.

[31] Á.B. Höskuldsson, Y. Abghoui, A.B. Gunnarsdóttir, E. Skúlason, Computational screening of rutile oxides for electrochemical ammonia formation, ACS Sustain. Chem. Eng. 5 (2017) 10327–10333, https://doi.org/10.1021/acssuschemeng.7b02379.

[32] X. Hu, Y. Sun, S. Guo, J. Sun, Y. Fu, S. Chen, S. Zhang, J. Zhu, Identifying electrocatalytic activity and mechanism of Ce₁/₃NbO₃ perovskite for nitrogen reduction to ammonia at ambient conditions, Appl. Catal. B: Environ. 280 (2021), 119419, https://doi.org/10.1016/j.apcatb.2020.119419.

[33] Y. Zhang, C.X. Harris, P. Wallenmeyer, J. Murowchick, X. Chen, Asymmetric lattice vibrational characteristics of rutile TiO₂ as revealed by laser power dependent Raman spectroscopy, J. Phys. Chem. C 117 (2013) 24015–24022, https://doi.org/10.1021/jp406948e.

[34] A. Wypych, I. Bobowska, M. Tracz, A. Opasinska, S. Kadlubowski, A. Krzywania-Kaliszewska, J. Grobelny, P. Wojciechowski, Dielectric properties and characterisation of titanium dioxide obtained by different chemistry methods, J. Nanomater. 2014 (2014) 1–9, https://doi.org/10.1155/2014/124814.

[35] K. Alamelu, V. Raja, L. Shiamala, B.M. Jaffar Ali, Biphasic $TiO_2$ nanoparticles decorated graphene nanosheets for visible light driven photocatalytic degradation of organic dyes, Appl. Surf. Sci. 430 (2018) 145–154, https://doi.org/10.1016/j.apsusc.2017.05.054.

[36] W. Zhang, H. Guo, H. Sun, R.-C. Zeng, Hydrothermal synthesis and photoelectrochemical performance enhancement of $TiO_2$/graphene composite in photo-generated cathodic protection, Appl. Surf. Sci. 382 (2016) 128–134, https://doi.org/10.1016/j.apsusc.2016.04.124.

[37] S. Wang, S. Zhou, Photodegradation of methyl orange by photocatalyst of CNTs/P-$TiO_2$ under UV and visible-light irradiation, J. Hazard. Mater. 185 (2011) 77–85, https://doi.org/10.1016/j.jhazmat.2010.08.125.

[38] M. Karuppannan, Y. Kim, S. Gok, E. Lee, J.Y. Hwang, J.-H. Jang, Y.-H. Cho, T. Lim, Y.-E. Sung, O.J. Kwon, A highly durable carbon-nanofiber-supported Pt–C core–shell cathode catalyst for ultra-low Pt loading proton exchange membrane fuel cells: facile carbon encapsulation, Energy Environ. Sci. 12 (2019) 2820–2829, https://doi.org/10.1039/C9EE01000A.

[39] S. Yurdakal, C. Garlisi, L. Özcan, M. Bellardita, G. Palmisano, (Photo)catalyst characterization techniques, in: Heterogeneous Photocatalysis, Elsevier, 2019, pp. 87–152, https://doi.org/10.1016/B978-0-444-64015-4.00004-3.

[40] H.Y.F. Sim, J.R.T. Chen, C.S.L. Koh, H.K. Lee, X. Han, G.C. Phan-Quang, J.Y. Pang, C.L. Lay, S. Pedireddy, I.Y. Phang, E.K.L. Yeow, X.Y. Ling, ZIF-induced d-band modification in a bimetallic nanocatalyst: achieving over 44% efficiency in the ambient nitrogen reduction reaction, Angew. Chem. 132 (2020) 17145–17151, https://doi.org/10.1002/ange.202006071.

[41] W. Fang, J. Zhao, T. Wu, Y. Huang, L. Yang, C. Liu, Q. Zhang, K. Huang, Q. Yan, Hydrophilic engineering of VOx -based nanosheets for ambient electrochemical ammonia synthesis at neutral pH, J. Mater. Chem. A 8 (2020) 5913–5918, https://doi.org/10.1039/D0TA00676A.

[42] F. Lai, N. Chen, X. Ye, G. He, W. Zong, K.B. Holt, B. Pan, I.P. Parkin, T. Liu, R. Chen, Refining energy levels in $ReS_2$ nanosheets by low-valent transition-metal doping for dual-boosted electrochemical ammonia/hydrogen production, Adv. Funct. Mater. 30 (2020), 1907376, https://doi.org/10.1002/adfm.201907376.

[43] W. Peng, M. Luo, X. Xu, K. Jiang, M. Peng, D. Chen, T. Chan, Y. Tan, Spontaneous atomic ruthenium doping in $Mo_2CT_X$ MXene defects enhances electrocatalytic activity for the nitrogen reduction reaction, Adv. Energy Mater. 10 (2020), 2001364, https://doi.org/10.1002/aenm.202001364.

[44] G. Lui, J.-Y. Liao, A. Duan, Z. Zhang, M. Fowler, A. Yu, Graphene-wrapped hierarchical $TiO_2$ nanoflower composites with enhanced photocatalytic performance, J. Mater. Chem. A 1 (2013) 12255, https://doi.org/10.1039/c3ta12329d.

[45] S. Yoshimaru, M. Sadakiyo, A. Staykov, K. Kato, M. Yamauchi, Modulation of the catalytic activity of Pt nanoparticles through charge-transfer interactions with metal–organic frameworks, Chem. Commun. 53 (2017) 6720–6723, https://doi.org/10.1039/C7CC02829F.

[46] L. Shi, Y. Yin, S. Wang, X. Xu, H. Wu, J. Zhang, S. Wang, H. Sun, Rigorous and reliable operations for electrocatalytic nitrogen reduction, Appl. Catal. B: Environ. 278 (2020), 119325, https://doi.org/10.1016/j.apcatb.2020.119325.

[47] P.A. Cox, F.W.H. Dean, A.A. Williams, Electrostatic models for surfaces of ionic crystals, Vacuum 33 (1983) 839–841, https://doi.org/10.1016/0042-207X(83)90622-X.

[48] Á.B. Höskuldsson, Y. Abghoui, A.B. Gunnarsdóttir, E. Skúlason, Computational screening of rutile oxides for electrochemical ammonia formation, ACS Sustain. Chem. Eng. 5 (2017) 10327–10333, https://doi.org/10.1021/acssuschemeng.7b02379.

[49] M. Yu, D.R. Trinkle, Accurate and efficient algorithm for Bader charge integration, J. Chem. Phys. 134 (2011), 064111, https://doi.org/10.1063/1.3553716.

[50] R. Sun, C. He, L. Fu, J. Huo, C. Zhao, X. Li, Y. Song, S. Wang, Defect engineering for high-selection-performance of NO reduction to $NH_3$ over $CeO_2$ (111) surface: a DFT study, Chin. Chem. Lett. (2021), https://doi.org/10.1016/j.cclet.2021.05.072.

[51] L. Fu, R. Wang, C. Zhao, J. Huo, C. He, K.-H. Kim, W. Zhang, Construction of Cr-embedded graphyne electrocatalyst for highly selective reduction of $CO_2$ to $CH_4$: a DFT study, Chem. Eng. J. 414 (2021), 128857, https://doi.org/10.1016/j.cej.2021.128857.

[52] J.-C. Liu, X.-L. Ma, Y. Li, Y.-G. Wang, H. Xiao, J. Li, Heterogeneous $Fe_3$ single-cluster catalyst for ammonia synthesis via an associative mechanism, Nat. Commun. 9 (2018) 1610, https://doi.org/10.1038/s41467-018-03795-8.